

Electric Current Induced Ultrafast Demagnetization

R. B. Wilson^{1,2,3,*}, Yang Yang^{4,*}, Jon Gorchon², Charles-Henri Lambert¹, Sayeef

Salahuddin^{1,2}, Jeffrey Bokor^{1,2}.

1) Department of Electrical Engineering and Computer Sciences, University of California, Berkeley, CA 94720, USA

2) Lawrence Berkeley National Laboratory, 1 Cyclotron Road, Berkeley, CA 94720, USA

3) Department of Mechanical Engineering and Materials Science and Engineering Program, University of California, Riverside, CA 92521, USA

4) Department of Materials Science and Engineering, University of California, Berkeley, CA 94720, USA

*denotes equal contributions

correspondence should be addressed to rwilson@engr.ucr.edu and jbokor@berkeley.edu.

Introduction

The pioneering observation of ultrafast demagnetization in ferromagnetic nickel following optical irradiation ¹ has led to the discovery of a broad range of extraordinary magnetic phenomena. Laser irradiation of magnetic metals can launch precessional modes at frequencies ranging from a few to hundreds of GHz ^{2,3}, drive ultrafast magnetic phase transitions ⁴, and generate enormous pure spin-currents ⁵⁻¹¹. Optical irradiation of ferrimagnetic systems such as GdFeCo and TbFeCo can result in an ultrafast reversal of the direction of magnetization¹²⁻¹⁴. Several studies have observed the response of magnetic metals to free-space THz radiation^{15,16}. Optically driven magnetic phenomena have potential applications for technologies such as data storage

and manipulation ¹³, or quantum computing ¹⁷. However, despite many significant scientific discoveries, the field of ultrafast magnetism has not yet led to the development of new technologies. The ability to directly induce ultrafast dynamics with electrical pulses could significantly broaden the technological utility of the field of ultrafast magnetism. Here, we show that electrical current can drive ultrafast magnetization dynamics. Using photoconductive Auston switches ¹⁸, we generate electrical pulses with 5 picosecond duration and hundreds of pJ of energy. The electrical pulse heats the electrons in the ferromagnet and causes ultrafast demagnetization of approximately one percent. An energy density of 25 MJ m^{-3} is required to induce 1% demagnetization, which compares favorably with the energy requirements for emerging nonvolatile memories ¹⁹. Therefore, the ability to induce ultrafast magnetization dynamics with electrical pulses offers a new pathway for spintronic devices operating with speeds in the few picosecond range.

Our experiments also provide new insight into the critical role that a nonthermal distribution of electrons plays in optically induced ultrafast demagnetization. We are able to deposit equal amounts of total energy into the electrons of a magnetic film by either optical or electrical heating. However, optical heating does so by exciting a few electrons $\sim 1.5 \text{ eV}$ above the Fermi-level. In contrast, electrical heating simultaneously excites many electrons a few meV above the Fermi level. As a result of the different

number of initially excited electrons, we observe significant differences in the magnetization dynamics induced by optical vs. electrical heating of a ferromagnet. We attribute the distinct dynamics that arise from electrical heating to enhanced electron-phonon scattering rates the result in more rapid electron cooling.

Main Text

We excite 5 picosecond electrical pulses on a coplanar waveguide structure (Fig. 1) using photoconductive Auston switches (Fig. 1b). Additional details concerning device properties and fabrication are in Supplemental Note 1-3 and Supplementary Figures 1-3. The energy carried by the electrical pulses, $\int I^2(t)Z_0 dt$, ranges from 1 to 200 pJ for DC biases across the photoswitch between 10 and 80 V. Fig. 1d shows the current profile $I(t)$. The impedance Z_0 of the waveguide is ~58 ohms. A small section of the CPW center line is made of a ferromagnetic thin film, see Fig. 1c. Upon passing through the ferromagnetic wire, the electrical pulse deposits ~10% of its energy via Joule heating, thereby inducing ultrafast demagnetization.

We performed both optical and electrical ultrafast demagnetization experiments on two Co/Pt multilayers (Fig. 2). The geometry of the first and second film are (3 nm Ta / 15 nm Pt / [0.7 nm Pt / 0.6 nm Co] x 8 / 5 nm Pt), and (1 nm Ta / 1 nm Pt / [0.7 nm

Pt / 0.86 nm Co] x 8 / 1.7 nm Pt), respectively. Below, we refer to these as the Pt/CoPt and the CoPt sample, respectively.

Figures 2 and 3 show the response of the two CoPt films to ultrafast heating of the electrons via optical (Fig. 2) and electrical pulses (Fig. 3a and 3b). For both types of heating, the magnetization decreases rapidly. However, clear differences exist. We attribute the differences to the initial distribution of excited electrons. Optical heating excites a nonthermal distribution. Electrical heating excites a thermal distribution.

Optical irradiation excites electrons between 0 and 1.55 eV above the Fermi level and the initial distribution is nonthermal, i.e. can't be described with Fermi-Dirac statistics^{20,21}. The excited electrons then relax to a thermal distribution via electron-electron scattering, electron-phonon scattering, and scattering between the electrons and spin degrees-of-freedom⁸. Scattering between the electronic and spin degrees-of-freedom of the metal increases populations of spin excitations, e.g. magnons, spin-density fluctuations, and Stoner excitations^{22,23}. As a result, ultrafast heating of the electrons rapidly decreases the total magnetization (Fig. 2).

We model the redistribution of energy from optically excited electrons to phonons and spin degrees-of-freedom with a phenomenological three temperature model^{1,23}, see Fig. 2 and Supplementary Note 4. The model possesses three fit parameters, the electron-phonon coupling constant $g_{ep} = 7 \times 10^{17} \text{ W m}^{-3} \text{ K}^{-1}$, the electron-spin coupling

constant $g_{es} = 5 \times 10^{17} \text{ W m}^{-3} \text{ K}^{-1}$, and the temperature dependence of the magnetization $1/M (dM / dT) \approx 10^{-3} \text{ K}^{-1}$.

The three temperature model ignores the initial nonthermal distribution of excited electrons ²¹. However, the initial nonthermal distribution persists for hundreds of femtoseconds in transition metals such as Al ²¹, Au ²⁰, Ni ²⁴, and Fe ²⁵ and will influence the response of a magnet to ultrafast heating. The high average energy of excitations in a nonthermal distribution may allow the generation of nonthermal spin excitations, e.g. Stoner excitations with sub-eV energies ²⁴. A nonthermal distribution of excited electrons can also impact how energy and angular momentum are transported, e.g. allow for superdiffusive spin and heat currents ^{5,6}.

Scattering theory predicts that whether the distribution of excited electrons is thermal or nonthermal impacts the rate of energy exchange between the electrons and lattice ²¹. The scattering rate between the electrons and phonons is proportional to the number of electronic excitations ²¹. The total number of electrons excited above the Fermi level increases by orders of magnitude after the absorbed energy is redistributed from a nonthermal to a thermal distribution via electron-electron scattering ²¹. Therefore, a nonthermal distribution of excited electrons will take hundreds of femtoseconds longer to equilibrate with the lattice than if the initial distribution is thermal. This prediction has been supported indirectly by comparing the value of g_{ep} derived from pump/probe

measurements to theory ^{21,26}. The value of g_{ep} derived by fitting pump/probe measurements with a thermal model are typically lower than theory predictions, presumably in order to compensate for the lower electron/phonon scattering rate while the electron distribution is nonthermal ²¹.

In addition to influencing the rate of energy transfer to phonons, there are a number of ways for a nonthermal distribution to influence demagnetization. For example, Elliot-Yafet scattering is thought to play a central role in ultrafast demagnetization ²⁷ and depends on the total electron-phonon scattering rate. The scattering rate between electrons and spin-excitations ⁸, e.g. magnons, may also depend on the number of excited electrons. Finally, the rate that electrons thermalize with the lattice will indirectly impact the magnetization dynamics. The rate of energy transfer to the spin degrees-of-freedom depends on how long the electrons remain hot ²³. A faster exchange of energy between electrons and phonons favors slower demagnetization ²³.

In contrast to optical heating, when electrons are electrically heated their energies only increase a few meV. The largest longitudinal electric field that occurs in the ferromagnetic wire during our experiments is $j_{\max} / \sigma \approx 4 \text{ MV m}^{-1}$, where j_{\max} is the maximum current density and σ is the electrical conductivity of the ferromagnet. Assuming a scattering time of $\sim 30 \text{ fs}$, a value typical for transition metals ²⁸, the

average increase in kinetic energy of an electron due to acceleration in the electric field prior to scattering is $\Delta E \approx (eE\tau)^2 / (2m_e) \approx 1 \text{ meV}$, where m_e is the mass of an electron. Because $\Delta E \ll k_B T$, the distribution of excited electrons is thermal. Therefore, by comparing the response of CoPt and Pt/CoPt to optical vs. electrical heating, we directly probe the impact of an initially nonthermal vs. thermal electron distribution on the magnetization dynamics.

Demagnetization of the CoPt following optical heating, as shown in Fig. 2, displays “type I” dynamics²⁷. The sample demagnetizes during laser irradiation, followed by a smaller increase in the magnetization as the electrons and phonons thermalize. Our “type I” categorization agrees with prior studies of Co/Pt²⁹, whose large spin-orbit coupling is credited with abnormally strong coupling between electronic and spin degrees-of-freedom. Magnetization dynamics without a recovery in the magnetization in the picoseconds following irradiation are “type II” dynamics²⁷. (The category of “type II” dynamics also includes observations of demagnetization on multiple time scales, as is observed for Gd²⁷.)

In contrast to the “type I” dynamics displayed following optical irradiation, the magnetization of neither CoPt or Pt/CoPt display a significant recovery in the picoseconds following heating (Fig. 3). Furthermore, the three-temperature model predictions do not agree with the experiment if we use the coupling constants derived

from fits to the optical experiments, $g_{ep} = 7 \times 10^{17} \text{ W m}^{-3} \text{ K}^{-1}$ and $g_{es} = 5 \times 10^{17} \text{ W m}^{-3} \text{ K}^{-1}$.

¹. This disagreement is due to the three-temperature model not accounting for the initial nonthermal distribution of excited electrons in the optical experiments.

The value of g_{ep} we derive for Pt/Co from optical experiments differs by a factor of two from our estimates of g_{ep} from theory. According to scattering theory ³⁰, $g_{ep} \approx \pi \hbar D_f \lambda \langle \omega^2 \rangle$, where \hbar is the reduced Planck's constant, k_B is Boltzmann's constant, D_f is the density of states at the Fermi level, λ is the electron-phonon coupling constant in the Eliashberg generalization of BCS theory, and $\langle \omega^2 \rangle$ is the second frequency moment of the phonons. We approximate $\langle \omega^2 \rangle$ by assuming a Debye density of states, $\langle \omega^2 \rangle \approx 0.6 \cdot k_B^2 \Theta_D^2 / \hbar^2$, where Θ_D is the Debye temperature. For Pt, $D_f \sim 9 \times 10^{47} \text{ J}^{-1} \text{ m}^{-3}$ ³¹, $\lambda = 0.66$ ³², and $\Theta_D \approx 240 \text{ K}$. Therefore, theory predicts $g_{ep} \approx 1.5 \times 10^{18} \text{ W m}^{-3} \text{ K}^{-1}$.

Three temperature model predictions agree with the electrically induced demagnetization data once we use the value of g_{ep} predicted by theory. In Fig. 3a and 3b, we show three temperature model predictions with $g_{ep} \sim 1.5 \times 10^{18} \text{ W m}^{-3} \text{ K}^{-1}$, the value for the electron-phonon coupling constant predicted for Pt ^{30,32}. We use the theory prediction for g_{ep} of Pt only because no experimental measurement of λ exists for Co.

We leave the ratio g_{es} / g_{ep} equal to what we derived from the optical experiments, consistent with prior studies that credit demagnetization to Elliot-Yafet scattering²⁷. However, the model predictions are not sufficiently sensitive to g_{es} to draw conclusions concerning electron-spin scattering rates for thermal vs. nonthermal distributions.

To determine the energy required for electrical demagnetization, we calculate the energy transferred to the electrons from the electrical pulse with a multilayer calculation of the frequency-dependent absorption coefficient³³, see Supplemental Note 5 and Supplementary Figure 4. Approximately 8% of the pulse's energy is absorbed while passing through the Pt/CoPt wire. We compare our model predictions to our observations for Pt/CoPt in Fig. 4. To generate 1% demagnetization of the Pt/CoPt requires ~ 14 pJ of energy.

The electrical energy required to induce ultrafast demagnetization of the ferromagnetic wire compares favorably with energy consumption of next generation memories. Many nonvolatile memory devices that are currently being aggressively researched, e.g. spin transfer torque magnetic memories or phase change memories, require sub-pJ energies per operation¹⁹. In our experiments on the Pt/CoPt wire, approx. 14 pJ of energy is needed to cause ~1% demagnetization, corresponding to an energy density of 25 MJ m⁻³. Therefore, for dimensions comparable to what they would be in a working device, e.g. (20 nm)³, energy requirements scale to ~0.25 fJ per 1%

demagnetization. For context, observations of ~10% demagnetization are typical in the ultrafast magnetism studies described in the opening paragraph ³⁴. Furthermore, all optical switching in ferrimagnets occurs when the optical energy absorbed is sufficient to cause ~50% demagnetization ³⁵. Therefore, if electronic devices are developed that utilize electrically induced ultrafast demagnetization, they could require as little as a few fJ per operation.

In conclusion, we observe rapid demagnetization in Co/Pt wires due to picosecond electrical heating. We observe large differences in the demagnetization rates of Co/Pt for optical vs. electrical heating that we attribute to the initially nonthermal vs. thermal distributions of excited electrons. The ability to induce ultrafast demagnetization with electrical pulses will enable development of novel spintronic devices capable of utilizing a broad array of recently discovered ultrafast magnetism phenomena.

Methods

We use a coplanar waveguide device with an integrated Auston switch to induce electrical demagnetization in a ferromagnetic metal. Upon optical irradiation of the biased photoconductive switch with an 830 nm laser, a transient electrical pulse with a FWHM of ~5 ps is generated and propagates along the CPW (Fig. 1d). The repetition

rate of the laser is 80 MHz and the pulse duration of the beam irradiating the photoconductive switch is ~ 2.3 ps. The laser pulse energy used to excite the Auston switch is held fixed at ~ 1.5 nJ. To bias the photoconductive switch during operation, we connect one side of the CPW device to a DC voltage source. We connect the other side of the device to a 50 ohm input of a 6 GHz oscilloscope to monitor the current pulse, or is shorted for convenience during MOKE measurements of the electrically induced demagnetization caused by the electrical pulses.

Optical ultrafast demagnetization experiments are typically performed with laser fluences between $1\text{-}10\text{ J m}^{-2}$ ^{10,23,35}, corresponding to irradiation of the film with 0.1 to 1 nJ of energy across a $100\text{ }\mu\text{m}^2$ region. Our CPW device delivers similar energy densities with an electrical pulse to a ferromagnetic wire. At a distance of 0.5 mm from the photoconductive switch, the center line width of the CPW and gap distance between the center line and ground are tapered down from $\sim 30\text{ }\mu\text{m}$ to $\sim 5\text{ }\mu\text{m}$ over 0.6 mm. The ratio between the centerline width and gap distance is constant in order to keep the waveguide impedance constant at 58 ohms. In the narrowed region of the CPW, a $3\text{ }\mu\text{m}$ long section of the center line is made out of a thin film of a ferromagnetic metal. Therefore, we are able to deliver ~ 200 pJ electrical pulses to a $16\text{ }\mu\text{m}^2$ ferromagnetic thin film, i.e we can deliver $\sim 6\text{ J m}^{-2}$.

To characterize the magnetization response of the CoPt samples to energy deposited either optically or electrically, we used time-resolved measurements of the polar magneto-optical Kerr effect (TR-MOKE). The probe pulse duration is 300 femtoseconds. We show a schematic of the pump/probe system in Supplementary Figure 5.

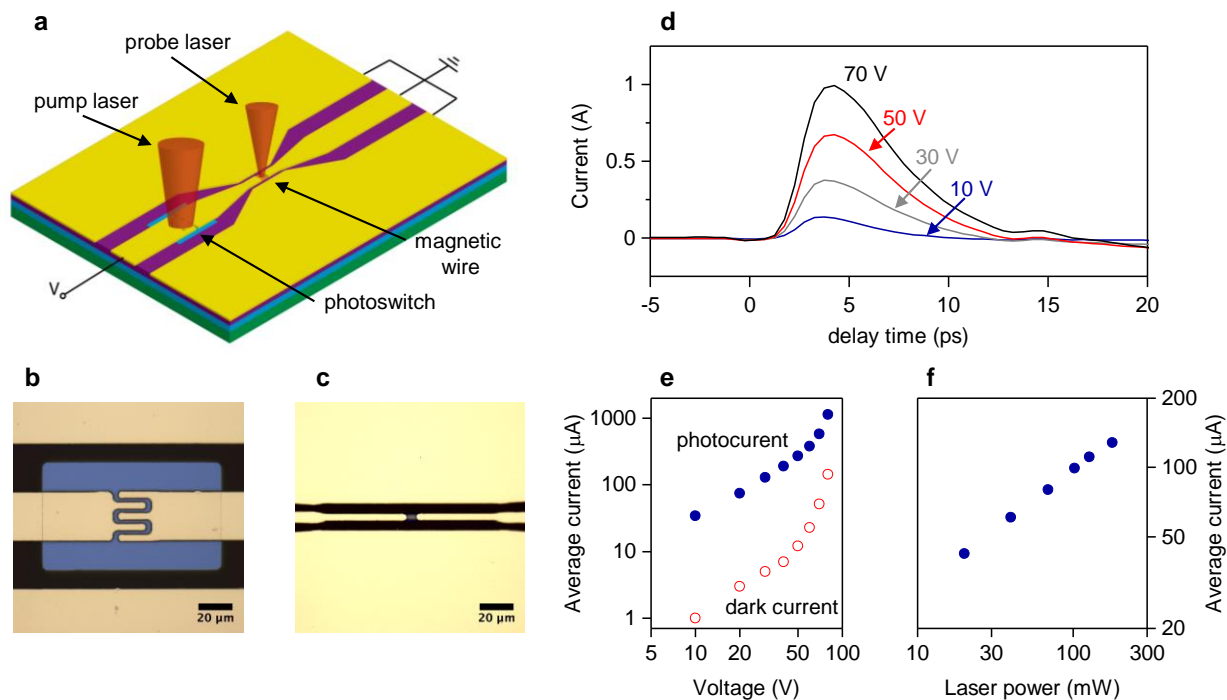


Figure 1. Device for electrically induced ultrafast demagnetization experiments.

a, Schematic of the electrical demagnetization experiments. The Auston switch is illuminated with a 1.5 nJ laser pulse while biased between 10 and 80 V. The magnetization of the magnetic wire is monitored via TR-MOKE. **b**, Optical image of the Auston switch. During illumination, photoexcited carriers in the low-temperature GaAs substrate conduct current across the gap, generating a transient electrical pulse that propagates along the waveguide towards a ferromagnetic section of the centerline. **c**, Optical image of the CoPt section of the waveguide. **d**, Temporal profile of the current pulse generated by the photoswitch, as measured with a Protomics probe positioned between the photoswitch and the CoPt wire. **e**, Average current across the device. The filled circles correspond to measurements while the photoswitch was irradiated with 1.5 nJ laser pulses at a rate of 80 MHz (photocurrent). Open circles are current measurements on the device without laser irradiation (dark current). A rapid increase in darkcurrent occurs as the bias voltage across the photoswitch approaches the breakdown voltage of the device, $\sim 90\text{V}$. **f**, Dependence of the average current on average laser power.

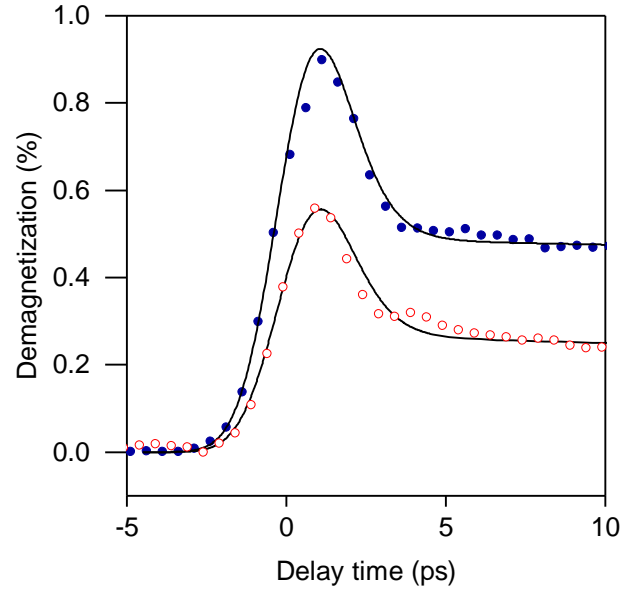


Figure 2. Optically induced demagnetization. Open markers are TR-MOKE measurements of the demagnetization of the Pt/CoPt multilayer following optical absorption of $\sim 0.2 \text{ J m}^{-2}$. Filled markers correspond to the demagnetization of the CoPt multilayer after optically absorbing $\sim 0.2 \text{ J m}^{-2}$. The solid lines are a three-temperature model prediction for the magnetization dynamics. A best fit to the data with the three-temperature model yields $g_{ep} = 7 \times 10^{17} \text{ W m}^{-3} \text{ K}^{-1}$. Both samples display a rapid demagnetization while the laser irradiates the sample, followed by a small recovery in the magnetization in the picoseconds following irradiation.

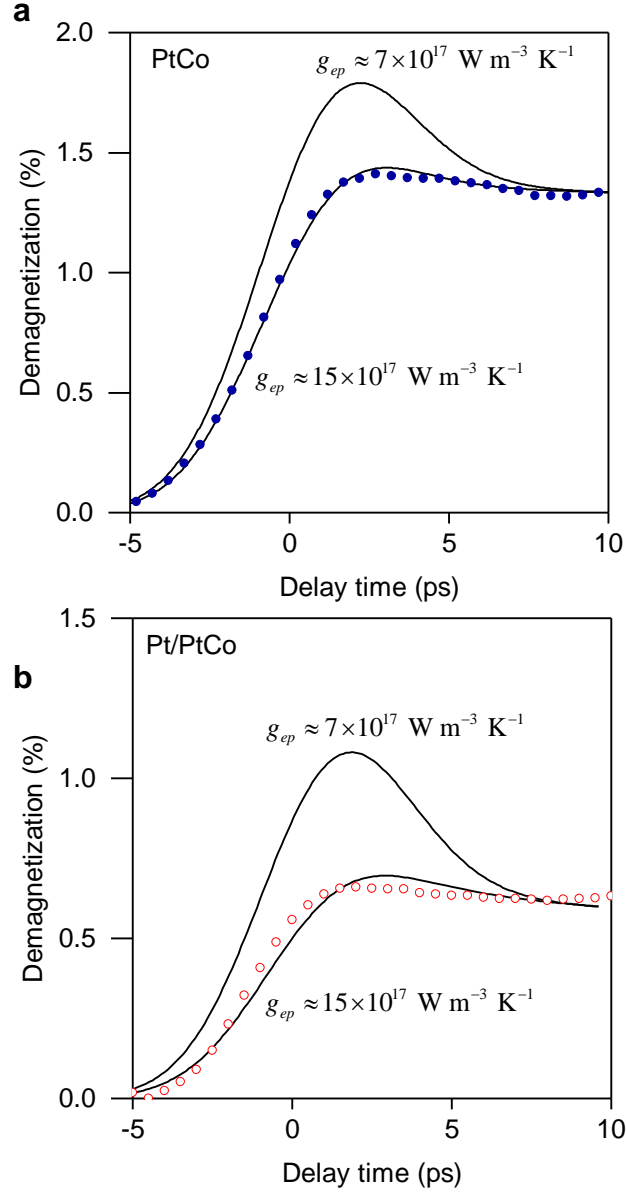


Figure 3. Electrically induced demagnetization. a, Filled markers are TR-MOKE measurements of the magnetization of the CoPt multilayer after heating by an electrical pulse with a 0.6 A peak amplitude. **b,** Open markers are TR-MOKE measurements of the Pt/CoPt multilayer heating by an electrical pulse with a 0.6 A peak amplitude. In both **(a,b)**, the solid lines are three-temperature model predictions for the demagnetization. We show model calculations using both the electron-phonon constant value derived from optical experiments ($g_{ep} = 7 \times 10^{17} \text{ W m}^{-3} \text{ K}^{-1}$, see Fig. 2), and calculated from theory ($g_{ep} = 15 \times 10^{17} \text{ W m}^{-3} \text{ K}^{-1}$, see main text). A higher rate of energy transfer between electrons and phonons in the electrical heating

experiments explains why there is no recovery of the magnetization in the picoseconds following electrical heating.

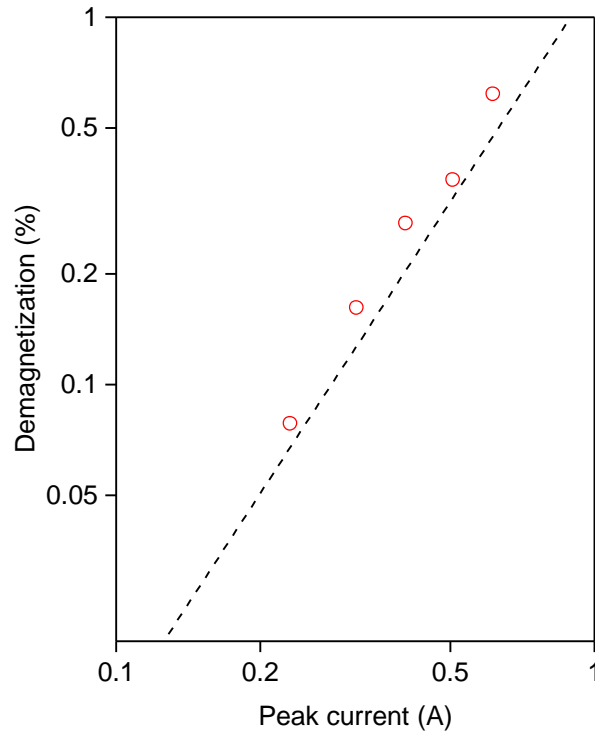


Figure 4. Demagnetization versus amplitude of the current pulse. Open markers are TR-MOKE measurements of the demagnetization 10 ps after the electrical pulse heats the Pt/CoPt. The dashed line are the predictions of our thermal model, using the value of $(1/M)dM/dT$ derived from optical demagnetization experiments and our estimate of energy absorbed by the electrons via joule heating, see Supplemental Information.

Acknowledgements

This work was primarily supported by the Director, Office of Science, Office of Basic Energy Sciences, Materials Sciences and Engineering Division, of the U.S. Department of Energy under Contract No. DE-AC02-05-CH11231 within the Nonequilibrium Magnetic Materials Program (MSMAG). We also acknowledge the National Science Foundation Center for Energy Efficient Electronics Science for providing most of the experimental equipment and partially supporting the fabrication of samples.

Author Contributions

R. B. W., Y.Y., J. G., designed the experiments under the supervision of J.B.. Y. Y. fabricated the devices with help from J. G. and C. L.. R.B.W., Y.Y., and J.G. performed the optical and electrical demagnetization experiments. C.L. sputtered the magnetic films under the supervision of S.S.. R.B.W. analyzed the experimental data with help from Y.Y. and J.G.. R.B.W. wrote the manuscript with input from all authors.

References

- 1 Beaurepaire, E., Merle, J. C., Daunois, A. & Bigot, J. Y. Ultrafast Spin Dynamics in Ferromagnetic Nickel. *Phys. Rev. Lett.* **76**, 4250-4253 (1996).
- 2 van Kampen, M. *et al.* All-Optical Probe of Coherent Spin Waves. *Phys. Rev. Lett.* **88**, 227201 (2002).
- 3 Becker, J. *et al.* Laser induced spin precession in highly anisotropic granular L10 FePt. *Appl. Phys. Lett.* **104**, 152412, doi:doi:<http://dx.doi.org/10.1063/1.4871869> (2014).
- 4 Ju, G. *et al.* Ultrafast Generation of Ferromagnetic Order via a Laser-Induced Phase Transformation in FeRh Thin Films. *Phys. Rev. Lett.* **93**, 197403 (2004).
- 5 Battiato, M., Carva, K. & Oppeneer, P. M. Superdiffusive Spin Transport as a Mechanism of Ultrafast Demagnetization. *Phys. Rev. Lett.* **105**, 027203 (2010).
- 6 Rudolf, D. *et al.* Ultrafast magnetization enhancement in metallic multilayers driven by superdiffusive spin current. *Nature communications* **3**, 1037 (2012).
- 7 Choi, G.-M., Min, B.-C., Lee, K.-J. & Cahill, D. G. Spin current generated by thermally driven ultrafast demagnetization. *Nature communications* **5** (2014).
- 8 Tveten, E. G., Brataas, A. & Tserkovnyak, Y. Electron-magnon scattering in magnetic heterostructures far out of equilibrium. *Phys. Rev. B* **92**, 180412 (2015).
- 9 Choi, G.-M. & Cahill, D. G. Kerr rotation in Cu, Ag, and Au driven by spin accumulation and spin-orbit coupling. *Phys. Rev. B* **90**, 214432 (2014).
- 10 Choi, G.-M., Moon, C.-H., Min, B.-C., Lee, K.-J. & Cahill, D. G. Thermal spin-transfer torque driven by the spin-dependent Seebeck effect in metallic spin-valves. *Nature Physics* **11**, 576-581 (2015).
- 11 Schellekens, A. J. & Koopmans, B. Microscopic model for ultrafast magnetization dynamics of multisublattice magnets. *Phys. Rev. B* **87**, 020407 (2013).
- 12 Ostler, T. A. *et al.* Ultrafast heating as a sufficient stimulus for magnetization reversal in a ferrimagnet. *Nat Commun* **3**, 666, doi:http://www.nature.com/ncomms/journal/v3/n2/supinfo/ncomms1666_S1.html (2012).
- 13 Liu, T.-M. *et al.* Nanoscale Confinement of All-Optical Magnetic Switching in TbFeCo - Competition with Nanoscale Heterogeneity. *Nano Letters* **15**, 6862-6868, doi:10.1021/acs.nanolett.5b02743 (2015).
- 14 Mangin, S. *et al.* Engineered materials for all-optical helicity-dependent magnetic switching. *Nat Mater* **13**, 286-292, doi:10.1038/nmat3864 (2014).
- 15 Bonetti, S. *et al.* THz-driven ultrafast spin-lattice scattering in amorphous metallic ferromagnets. *arXiv preprint arXiv:1604.04077* (2016).
- 16 Shalaby, M., Vicario, C. & Hauri, C. P. Low frequency terahertz-induced demagnetization in ferromagnetic nickel. *Appl. Phys. Lett.* **108**, 182903, doi:doi:<http://dx.doi.org/10.1063/1.4948472> (2016).
- 17 Kirilyuk, A., Kimel, A. V. & Rasing, T. Ultrafast optical manipulation of magnetic order. *Rev. Mod. Phys.* **82**, 2731-2784 (2010).
- 18 Smith, F. W. *et al.* Picosecond GaAs-based photoconductive optoelectronic detectors. *Appl. Phys. Lett.* **54**, 890-892, doi:doi:<http://dx.doi.org/10.1063/1.100800> (1989).
- 19 Wong, H. S. P. & Salahuddin, S. Memory leads the way to better computing. *Nat Nano* **10**, 191-194, doi:10.1038/nnano.2015.29 (2015).
- 20 Fann, W. S., Storz, R., Tom, H. W. K. & Bokor, J. Electron thermalization in gold. *Phys. Rev. B* **46**, 13592-13595 (1992).

- 21 Tas, G. & Maris, H. J. Electron diffusion in metals studied by picosecond ultrasonics. *Phys. Rev. B* **49**, 15046-15054 (1994).
- 22 Schmidt, A. B. *et al.* Ultrafast Magnon Generation in an Fe Film on Cu(100). *Phys. Rev. Lett.* **105**, 197401 (2010).
- 23 Kimling, J. *et al.* Ultrafast demagnetization of FePt:Cu thin films and the role of magnetic heat capacity. *Phys. Rev. B* **90**, 224408 (2014).
- 24 Scholl, A., Baumgarten, L., Jacquemin, R. & Eberhardt, W. Ultrafast Spin Dynamics of Ferromagnetic Thin Films Observed by fs Spin-Resolved Two-Photon Photoemission. *Phys. Rev. Lett.* **79**, 5146-5149 (1997).
- 25 Carpena, E. *et al.* Dynamics of electron-magnon interaction and ultrafast demagnetization in thin iron films. *Phys. Rev. B* **78**, 174422 (2008).
- 26 Waldecker, L., Bertoni, R., Ernstorfer, R. & Vorberger, J. Electron-Phonon Coupling and Energy Flow in a Simple Metal beyond the Two-Temperature Approximation. *Physical Review X* **6**, 021003 (2016).
- 27 Koopmans, B. *et al.* Explaining the paradoxical diversity of ultrafast laser-induced demagnetization. *Nature materials* **9**, 259-265 (2010).
- 28 Jin, Z. *et al.* Accessing the fundamentals of magnetotransport in metals with terahertz probes. *Nat Phys* **11**, 761-766, doi:10.1038/nphys3384 (2015).
- 29 Kuiper, K. *et al.* Spin-orbit enhanced demagnetization rate in Co/Pt-multilayers. *Appl. Phys. Lett.* **105**, 202402 (2014).
- 30 Allen, P. B. Theory of thermal relaxation of electrons in metals. *Phys. Rev. Lett.* **59**, 1460-1463 (1987).
- 31 Lin, Z., Zhigilei, L. V. & Celli, V. Electron-phonon coupling and electron heat capacity of metals under conditions of strong electron-phonon nonequilibrium. *Phys. Rev. B* **77**, 075133 (2008).
- 32 Allen, P. B. Empirical electron-phonon λ values from resistivity of cubic metallic elements. *Phys. Rev. B* **36**, 2920-2923 (1987).
- 33 Orfanidis, S. J. *Electromagnetic waves and antennas*. (Rutgers University New Brunswick, NJ, 2002).
- 34 Walowski, J. & Münzenberg, M. Perspective: Ultrafast magnetism and THz spintronics. *arXiv preprint arXiv:1606.08725* (2016).
- 35 Gorchon, J. *et al.* The role of electron temperature in the helicity-independent all-optical switching of GdFeCo. *arXiv preprint arXiv:1605.09764* (2016).
- 36 Matheisen, C., Nagel, M. & Sawallich, S. in *2015 40th International Conference on Infrared, Millimeter, and Terahertz waves (IRMMW-THz)*. 1-3.

Supplemental Note 1. Carrier lifetime in low temperature GaAs.

The LT-GaAs wafer, purchased from the company Pam-Xiamen, consists of a 1-micron thick GaAs layer grown at low temperature by molecular beam epitaxy on a GaAs substrate. Excess As in the LT-GaAs causes a short carrier lifetime due to a high density of point defects. Transient reflectivity measurements of the LT-GaAs are shown in Supplemental Figure 1 and indicate a carrier lifetime of ~ 2 ps in the LT-GaAs layer.

Supplemental Note 2. Sample Fabrication Process.

A schematic is shown in Supplemental Figure 2 of the device fabrication. The procedure involves three photolithography/lift-off steps. First, we cover the whole substrate, with the exception of a small area where the photoswitch will be located, with an insulating layer of MgO in order to increase the resistance between the signal and ground lines of the CPW. The ~100 nm of MgO is deposited via RF-Sputter onto the sample with an Ar/O₂ ratio of 16 to 1 at a pressure of 4.7 mT and power of 60 W. The dimensions of the patterned region where the MgO is lifted off from are 100um x 60um. After completing a second round of lithography, we deposit the magnetic section of the CPW center line using DC magnetron sputtering. The magnetic wire dimensions at this stage are 5 um wide x 20 um long. After a final photolithography step, we deposit Ti/Au layers that will form the transmission lines and photoswitch. The 250 nm thick Au transmission lines are deposited via e-beam evaporation. To promote adhesion, a 20 nm Ti layer is evaporated first onto the sample first. The Au center line of the CPW overlaps with a 8.5 um long by 5 um wide section of the magnetic wire on both sides. As a result, the final dimensions of the section of the magnetic wire that is uncoated with Ti and Au are 5 um x 3 um.

We use two layers of photoresist for all the photolithography steps prior to film deposition and lift-off. First, we spin coat a layer of LOR-5A (MicroChem) at 4100 RPM for 30s, followed by a bake at 150 °C for 10 min. Second, we spin coat the sample with a layer of OiR 906-12 (Dow Chemical) at 4100 RPM for 30 s followed by a soft bake at 90 °C for 1 min. To pattern the photoresist, we expose the sample to 130mJ cm⁻² with a Karl Suss MA6 Mask Aligner. Then, the sample is developed with OPD 4262 (Fujifilm) for 40s. Next, either an MgO, CoPt, or Ti/Au film is deposited. Finally, lift-off off the photo-resist is performed by soaking the sample in Remover PG (MicroChem) over 12 hours.

Supplemental Note 3. Measurement of Picosecond Current Pulses

We use a Protemics Teraspike probe to characterize the temporal profile of the electric field on the CPW device ³⁶. The Protemics probe consists of a 2 μm wide LT-GaAs Auston photo-switch that is positioned on the end of a flexible Polyethylene terephthal cantilever. We position the Protemics probe tip between the centerline and ground of the CPW at the region of interest of the sample see Supplementary Figure 3. A probe laser beam illuminates the tip. A linear delay stage controls the optical delay between the probe beam and the pump beam exciting the Auston switch on the sample. During probe beam illumination, the Protemics probe outputs a photocurrent proportional to the strength of the electric field between the centerline and ground plane of the CPW. By monitoring the photocurrent from the Protemics probe as a function of the optical delay between the pump and probe lasers, we map the temporal profile of the electric field at that location of the CPW. The sensitivity of the Protemics probe tip is ~ 150 pA per 1 V/m for a probe beam power on the probe tip of 1 mW. However, the sensitivity of the Protemics probe varies as much as factor of two between experiments. The variation depends on factors such as the angle between the cantilever and sample and the proximity between the probe surface and sample surface. We use the average photocurrent generated by the photoswitch, as measured by the DC voltage source to estimate the total charge contained in each pulse generated by the Auston switch.

Supplemental Note 4. Three Temperature Model.

The three temperature model is based on the assumption of three thermal reservoirs, electrons at temperature T_e , phonons at temperature T_p , and magnetization at temperature T_s . We assume that rate of energy transfer between the spin degrees-of-freedom and phonons is negligible. Furthermore, we assume that because of the short life-times of spin-excitations in ferromagnetic metals that the diffusion of heat in the spin reservoir is negligible. [19], Then, the three temperature model consists of three equations for each layer in the sample,

$$C_e \frac{dT_e}{dt} = g_{ep}(T_p - T_e) + g_{es}(T_s - T_e) + \Lambda_e \frac{d^2 T_e}{dx^2} + P(t, z), \quad (\text{S1})$$

$$C_p \frac{dT_p}{dt} = g_{ep}(T_e - T_p) + \Lambda_p \frac{d^2 T_p}{dx^2}, \quad (\text{S2})$$

$$C_s \frac{dT_s}{dt} = g_{es}(T_e - T_s). \quad (\text{S3})$$

Here, C denotes specific heat, g denotes energy transfer coefficient, Λ denotes thermal conductivity, and the subscripts e , p , and s refer to the thermodynamic reservoirs of electrons, phonons, and spin. The laser energy is transferred to the electron reservoir with a rate $P(t, z)$, which is calculated using a multilayer matrix method. The laser pulse duration was measured with an autocorrelator.

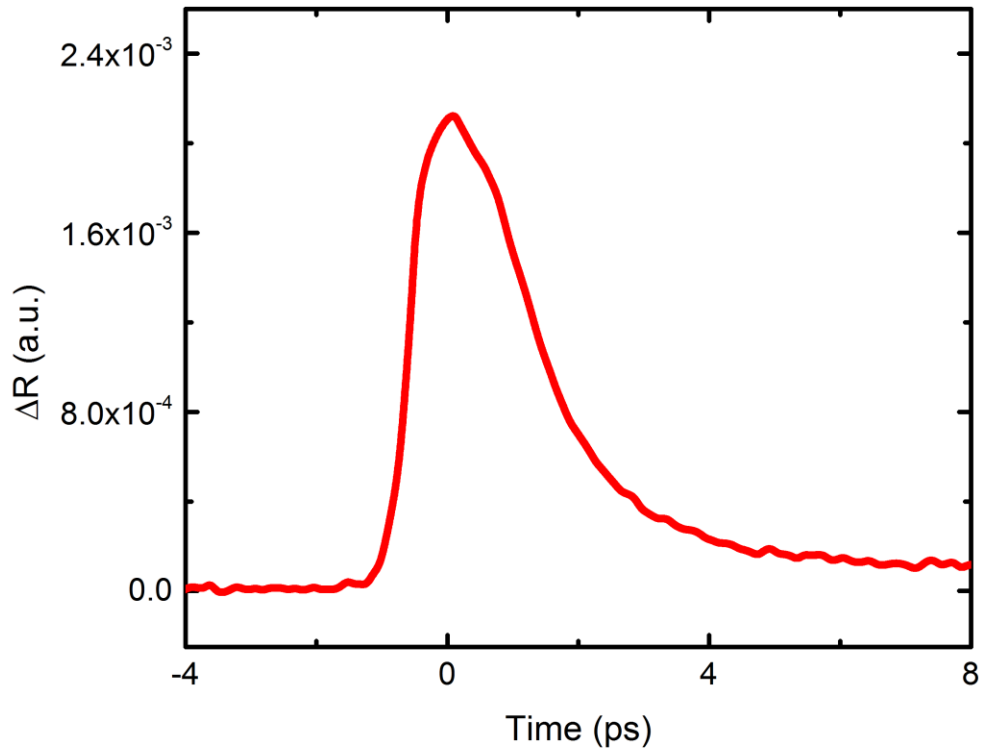
For the CoPt multilayer, we treat the entire stack as an effective medium. We set the electronic heat capacity to $0.15 \text{ MJ m}^{-3} \text{ K}^{-1}$ based on first principles calculations. We set the phonon heat capacity to $3.05 \text{ MJ m}^{-3} \text{ K}^{-1}$, a weighted average of the bulk values for Pt and Co. We set the spin heat capacity to $0.2 \text{ MJ m}^{-3} \text{ K}^{-1}$, the value of Nickel at room temperature which has a magnetization and Curie temperature as Co/Pt multilayers. The electronic thermal conductivity was fixed using the Wiedemann Franz law and measurements of the electrical

conductivity, $\rho = 7 \times 10^{-7} \Omega \text{ m}$. The phonon thermal conductivity was estimated to be $3 \text{ W m}^{-1} \text{ K}^{-1}$, a value typical for heavy metals.

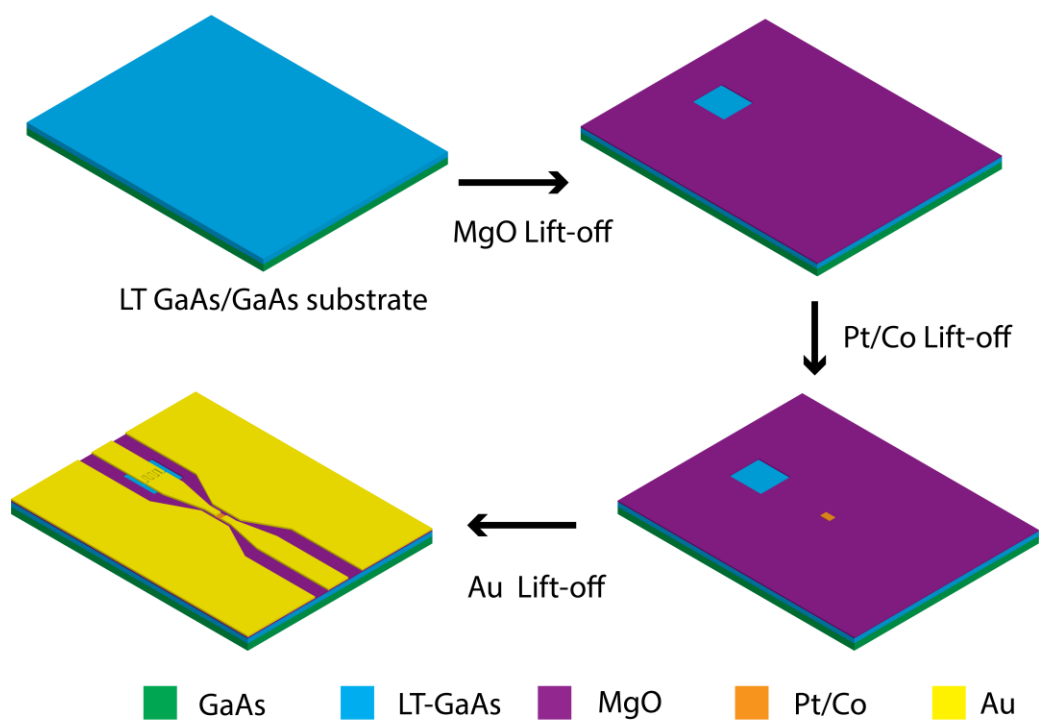
We treat the Pt/CoPt sample as a three-layer system: 5 nm Pt / 10.4 nm PtCo / 18 nm Pt. We set the thermal properties of the CoPt layer equal to those for the CoPt sample. We assumed a phonon and electrical interface conductance between samples of $300 \text{ MW m}^{-2} \text{ K}^{-1}$ and $10 \text{ GW m}^{-2} \text{ K}^{-1}$, both typical values phonon-phonon and electron-electron interface conductances. We set the Pt electron/phonon coupling constant to $35 \times 10^{17} \text{ W m}^{-3} \text{ K}^{-1}$ based on Ref. [1]. Finally, we set the electronic thermal conductivity of Pt using the Wiedemann Franz law, and an estimate of the electrical resistivity of $\rho = 3 \times 10^{-7} \Omega \text{ m}$ based on sheet resistance measurements.

Supplemental Note 5. Multilayer absorption calculations.

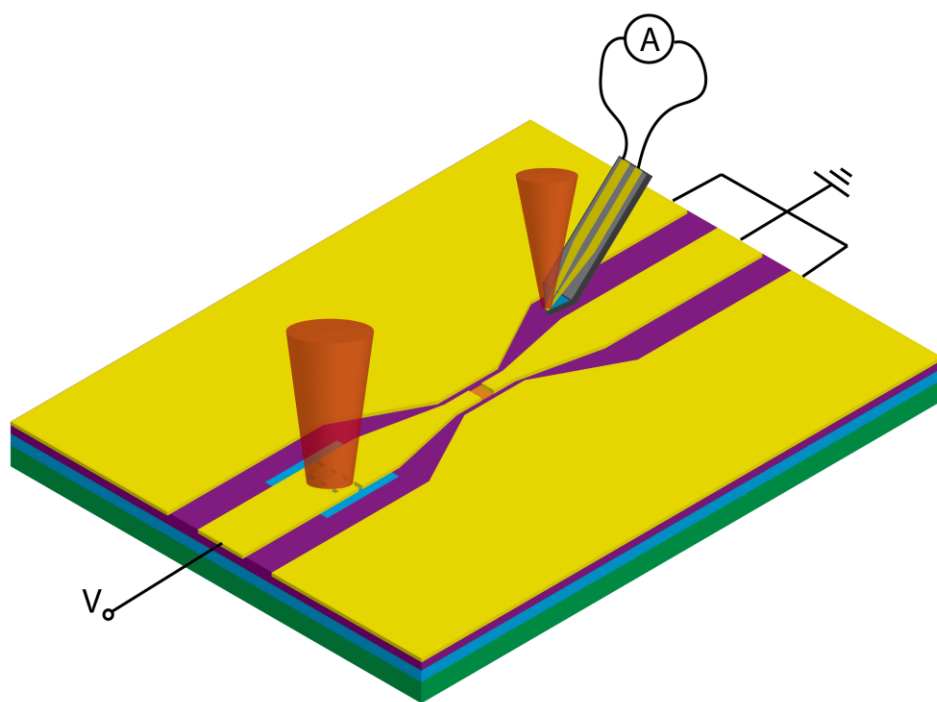
We calculate the energy transferred to the electrons by the electrical pulse with a multilayer reflectivity calculation of the frequency dependent absorption coefficient $\alpha(\omega)$ ³³. We calculate the energy absorbed from the electrical pulse via a weighted average of the frequency components in the picosecond pulse. We calculate the frequency dependence of the coplanar waveguide impedance using transmission line theory. In our calculation of the frequency dependent impedance, we neglect the frequency dependence of the Pt/CoPt electrical conductivity. Other similar materials, such as NiFe/Cu multilayers²⁸, display a relatively weak frequency dependence of the electrical conductivity at sub THz frequencies. Therefore, we expect that neglecting the frequency dependence of the conductivity of Pt/CoPt results in less than a 10% error in our calculation of the absorption coefficient. After calculating the frequency dependent impedance, we calculate the reflection, transmission, and absorption as a function of frequency for a 3 layer structure, Au CPW / Pt/CoPt CPW / Au CPW. We show the results of this calculation in Supplementary Figure 5. We approximate the amplitude of the electrical pulse's various frequency components by taking the Fourier transform of the current pulse, and calculate a weighted average. For simplicity, we approximate the picosecond pulse with a Gaussian function with a e^{-1} time constant of 2.3 ps. We note that the electrical heating is proportional to the current profile squared, and therefore contains higher frequency components than the current pulse. We conclude that ~8% of the electrical pulse energy is absorbed by the Pt/CoPt section of the waveguide. Together with the three temperature model described in Supplemental Note 4, we can predict the demagnetization we expect for various current amplitudes. We compare our model predictions for demagnetization with our observations for Pt/CoPt in Fig. 4.



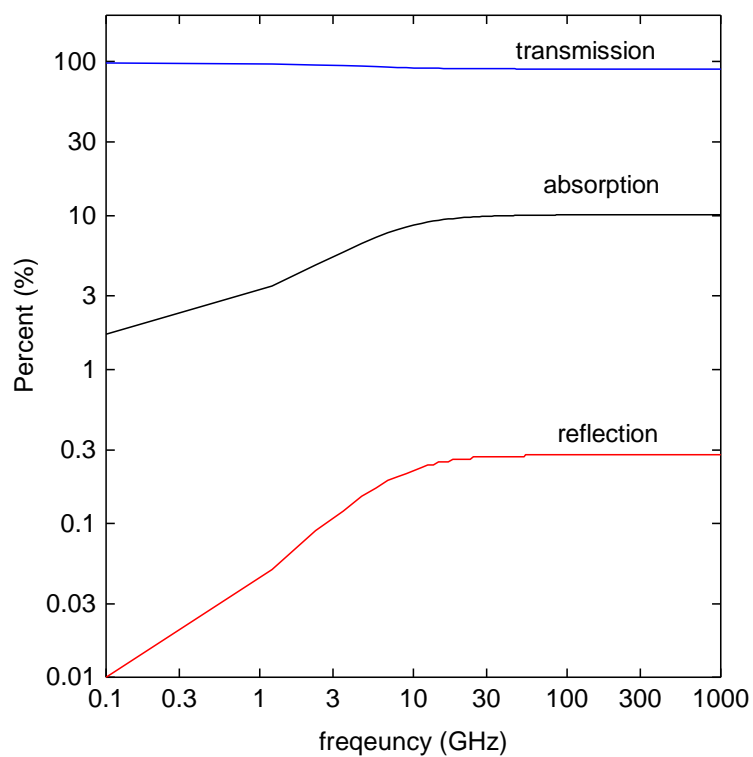
Supplemental Figure 1. Time domain reflectance measurement of LT-GaAs wafer. During optical irradiation, the excitement of electron-hole pairs causes a change in the reflectance. After laser irradiation ends, the transient reflectivity decays as electron-hole excitations relax. The decay of the transient reflectance reveals a ~ 2 ps life time for the optical excitations.



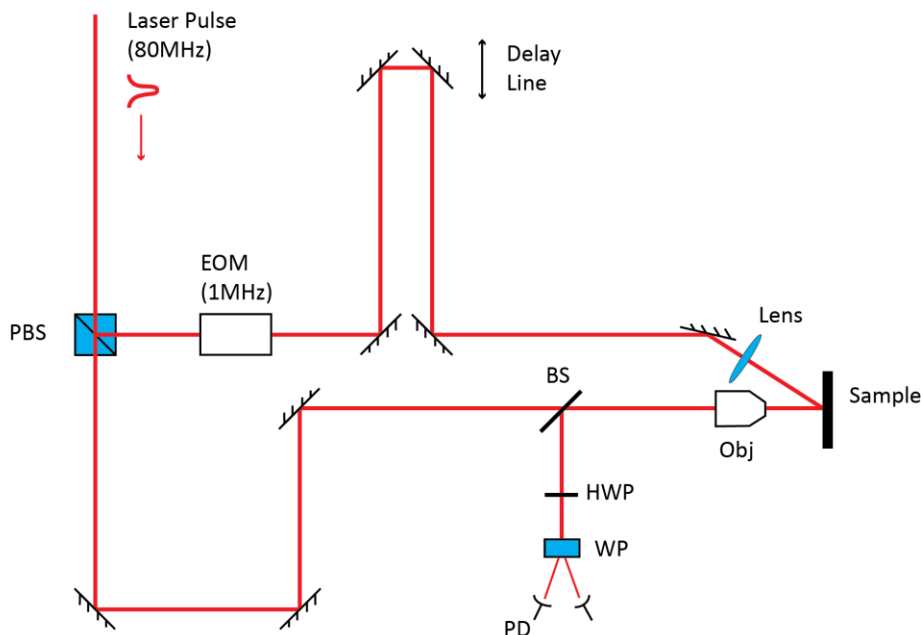
Supplemental Figure 2. Fabrication procedure for the coplanar waveguide devices.



Supplemental Figure 3. Schematic of the experimental setup for measuring the temporal profile of the electrical pulse.



Supplemental Figure 4. Calculation of the percent energy absorbed by the Pt/CoPt wire due to Joule heating.



Supplemental Figure 5. Schematic of the TR-MOKE setup. Red line indicates the laser beam path. PBS stands for polarizing beamsplitter, EOM is electro-optic modulator, BS is beamsplitter, Obj is a 20x objective, HWP is half-wave plate, WP is a Wollaston prism, and PD is photodetector. The same layout is used when using the Proteomics probe to characterize the electrical pulse on the CPW. The one difference is no reflected probe beam light is collected and focused on a photodetector. Instead, we monitor the photocurrent from the Proteomics probe.